Article:
Plane, JMC, Saunders, RW, Hedin, J et al. (10 more authors) (2014) A combined rocket-borne and ground-based study of the sodium layer and charged dust in the upper mesosphere. Journal of Atmospheric and Solar-Terrestrial Physics, 118B. 151 - 160. ISSN 1364-6826

https://doi.org/10.1016/j.jastp.2013.11.008

A combined rocket-borne and ground-based study of the sodium layer and charged dust in the upper mesosphere

John M. C. Plane[1], Russell W. Saunders[1],

Jonas Hedin[2], Jacek Stegman[2], Misha Khaplanov[2] and Jörg Gumbel[2]

Kristina A. Lynch[3], Phillip J. Bracikowski[3]

Lynette J. Gelinas[4]

Martin Friedrich[5]

Sandra Blindheim[6], Michael Gausa[6]

Bifford P. Williams[7]

[1] School of Chemistry, University of Leeds, UK

[2] MISU, Stockholm University, Sweden

[3] Department of Physics, Dartmouth University, US

[4] Aerospace Corporation, Los Angeles, US

[5] Technical University of Graz, Austria

[6] Andøya Rocket Range, Norway

[7] GATS-Inc, Boulder, US

Abstract

The Hotel Payload 2 rocket was launched on January 31st 2008 at 20.14 LT from the Andøya Rocket Range in northern Norway (69.31° N, 16.01° E). Measurements in the 75 - 105 km region of atomic O, negatively-charged dust, positive ions and electrons with a suite of instruments on the payload were complemented by lidar measurements of atomic Na and temperature from the nearby ALOMAR observatory. The payload passed within 2.58 km of the lidar at an altitude of 90 km. A series of coupled models is used to explore the observations, leading to two significant conclusions. First, the atomic Na layer and the vertical profiles of negatively-charged dust (assumed to be meteoric smoke particles), electrons and positive ions, can be modelled using a self-consistent meteoric input flux. Second, electronic structure calculations and Rice-Ramsperger-Kassel-Markus theory are used to show that even small Fe-Mg-silicates are able to attach electrons rapidly and form stable negatively-charged particles, compared with electron attachment to O_2 and O_3. This explains the substantial electron depletion between 80 and 90 km, where the presence of atomic O at concentrations in excess of 10^{10} cm^{-3} prevents the formation of stable negative ions.

1. Introduction

It was first suggested more than half a century ago that nano-particles form in the earth's upper atmosphere as a result of the ablation of meteoroids and the subsequent condensation of gas-phase metal oxide and silicate species (Rosinski and Snow, 1961, Hunten et al., 1980). Meteoric ablation is also the source of the layers of metal atoms - Na, Fe, Mg etc - which occur globally between 80 and 105 km in the

mesosphere/lower thermosphere (MLT) (Plane, 2003). Below about 85 km, these metals are converted to reservoir species - mainly hydroxides and carbonates - through reactions involving O_3, O_2, CO_2 and H_2O. Chemical ablation modelling indicates that similar quantities of iron, magnesium and silicon - the bulk constituents of chondritic meteoroids - are injected into the upper atmosphere (Vondrak et al., 2008). Laboratory experiments have shown that Fe and Mg oxides spontaneously polymerize with SiO_2 vapour to form nano-particles, principally of olivine composition ($Fe_{2-2x}Mg_{2x}SiO_4$, $0 \leq x \leq 1$) (Saunders and Plane, 2006, Saunders and Plane, 2011). In the mesosphere the formation of these so-called meteoric smoke particles (MSPs) occurs over several days, and is presumed to lead to the permanent removal of these metallic compounds from the gas phase.

MSPs can be measured directly above 70 km by rocket-borne particle detectors (e.g. Gelinas et al. (2005), Lynch et al. (2005) , Rapp et al. (2007), Robertson et al. (2013)). These measurements indicate typical particle numbers of a few thousand per cm^{-3} above 75 km. However, the detectors measure only those particles that are charged, so that the total MSP concentration has to be obtained by dividing the measured number by the fraction of charged particles in the plasma, which has to be estimated from a dusty plasma model. Because the plasma density in the region between 70 and 100 km varies from ~ 100 - 20,000 cm^{-3}, roughly similar to the number density of MSPs, the modelled fraction of charged MSPs depends on a number of parameters which are poorly known, such as electron-particle attachment rates and electron photo-detachment rates (Rapp et al., 2007).

In order to improve this situation, a new type of particle detector has been flown recently which contains a pulsed VUV lamp to photo-detach electrons from negatively charged particles (Rapp et al., 2010, Rapp et al., 2012). This has been

93 followed by the flight of an electrostatic multichannel mass analyzer, which can
94 measure several different mass ranges and both negatively- and positively-charged
95 particles (Robertson et al., 2013). The MSP number density and size have also been
96 estimated by analysing the backscatter signals from high performance-large aperture
97 radars (Fentzke et al., 2009), although this is a less direct technique. In addition, the
98 first optical detection of MSPs between ~ 40 and 80 km has now been reported, using
99 the SOFIE spectrometer on the AIM satellite (Hervig et al., 2009). Observations at
100 several wavelengths (near-UV to near-IR) have been used to infer that MSPs are
101 composed of amorphous metal silicates.

102 In this paper we will describe and then model a selection of results from the Hotel
103 Payload 2 (HotPay 2) project, which are relevant to understanding the neutral metal
104 layers in the MLT, the formation of meteoric smoke, and the effect of MSPs on the
105 plasma in the upper mesosphere. HotPay 2 was a complex sounding rocket project
106 managed and supported by the Andøya Rocket Range, Norway. The payload carried
107 instruments from nine scientific institutes in different European countries, and one
108 instrument from the US. The launch was supported by ground-based lidar, radar and
109 airglow measurements (Enell et al., 2011). Although the payload was designed to
110 study a number of upper atmospheric phenomena, including auroral physics, particle
111 precipitation and the cosmic ray flux, in this paper we will focus on the experiments
112 designed to study the MLT region.

113 There are two linked questions that we will address. First, can the atomic Na layer and
114 the MSP size distribution be accounted for self-consistently by the same meteoric
115 input flux? Second, is the attachment rate of electrons to very small MSPs large
116 enough to explain the substantial depletion of electrons relative to positive ions,
117 which is always observed between about 80 and 90 km (e.g. Friedrich et al. (2011))?

2. The HotPay 2 campaign

The HotPay 2 rocket was launched on January 31st 2008 at 20.14 LT from the Andøya Rocket Range in northern Norway (69.31^o N, 16.01^o E). The scientific conditions for the launch were excellent: a clear night for the ground-based optical instruments, and a stable auroral arc to the north. The payload reached an altitude of 380 km (target 342 km). The Na lidar at the ALOMAR observatory on a mountain behind the rocket range was successfully aimed to intersect the planned payload trajectory in the MLT region: the lidar was only 2.58 km from the payload as it passed through 90 km. The rocket was launched when the Na layer was observed to be relatively unperturbed i.e., close to an average Gaussian profile centred around 90 km (Figure 1), and there were quiet auroral conditions overhead. Further details concerning the payload, launch conditions and ancillary ground-based observations are described in Enell et al. (2011).

2.1 Airglow measurements

The vertical profile of atomic O was measured using an on-board O_2 Atmospheric band photometer. O atoms, which are mostly produced in the upper atmosphere through O_2 photolysis during the day, recombine to form molecular O_2 in a number of metastable states which can then emit radiation. One of the strongest emission features in the night sky spectrum is the Atmospheric Band system $\left(b^1\Sigma_g^+ \rightarrow X^3\Sigma_g^-\right)$ dominated by the (0-0) and (0-1) bands at 762 nm and 864 nm, respectively. The 762 nm nightglow emission was measured on HotPay 2 using a standard filter photometer

which was one of three comprising the Night-Time Emissions from the Mesosphere and Ionosphere (NEMI) instrument on the top deck of the payload (Enell et al., 2011). The resulting profile was then numerically differentiated to yield the volume emission rate of the emitting layer, which was converted into the absolute atomic O concentration using the formalism developed from the ETON (Energy Transfer in the Oxygen Nightglow) rocket campaign in 1982 (Greer et al., 1986). In that study the atomic oxygen density and O_2 Atmospheric band airglow intensity were measured simultaneously, from which a consistent set of reaction rates describing the O_2 nightglow excitation processes and quenching mechanisms could be derived (Murtagh, 1989, Hedin et al., 2009). Further details of the instrument and analysis procedure are described elsewhere (Enell et al., 2011). The derived O concentration density profile is shown in Figure 1.

2.2 Plasma measurements

The payload carried two separate instruments for the determination of plasma constituent densities: a three-frequency radio wave propagation experiment to obtain electron densities by the Faraday rotation technique, and a gridded electrostatic probe to measure positive ions (Enell et al., 2011, Friedrich et al., 2012). The wave propagation experiment consisted of ground-based transmitters for each frequency (2.20, 3.88 and 15.01 MHz) radiating linearly polarised waves to the rocket payload. The payload carried receivers for these frequencies fed from a common linearly polarised antenna. For reasons of flight stability, HotPay 2 had a spin-rate of 3.3 rps, which also rotated the antenna. With this configuration the received signals have two maxima and two minima each spin period, i.e. whenever the antenna was parallel and

perpendicular, respectively, to the transmitting antenna on the ground. In the presence of a magnetic field the electron density content between transmitter and receiver leads to a rotation of the polarisation i.e. Faraday rotation. This rotation (phase against an aspect sensor) is the raw data from which electron content and, in consequence, electron density is derived. The height resolution is limited by the rocket spin with which the wave polarisation is scanned, but the measurements are completely immune to payload charging or aerodynamic effects. This method is described e.g. by Bennett et al. (1972), and the choice of sounding frequencies was addressed by Jacobsen and Friedrich (1979).

The ion probe consisted of a gridded sphere at plasma/payload potential with a negatively biased collector inside. Such an arrangement measures a current primarily determined by the relative velocity between probe and plasma (i.e. the rocket velocity), the probe's cross section, its transparency and the ambient ion number density. The current contribution due to the thermal velocity of the ions was considered in the data processing, but constitutes only a marginal correction since the rocket's velocity always considerably exceeded the thermal velocity of the ions. Similarly, the payload potential is less crucial for this probe than e.g. for a Langmuir probe where its potential directly determines the collected current (Sagalyn and Smiddy, 1963, Blix et al., 1990). On Hotpay 2 the probe was mounted on a rigid boom on the uppermost deck and thus observed negligible spin modulation, yielding ion densities with good height resolution. Figure 2 illustrates the resulting profiles of ion and electron density.

2.3 Charged dust measurements

The Dartmouth College Dust Detector (Lynch et al., 2005) is a Faraday cup designed to collect charged MSPs in the mesosphere. Because of the rocket's ram velocity, particles are driven through a series of ground, bias, and rejection screens at the front of the detector. The rejection screen is used to prevent the collection of thermal electrons with 1eV or less energy. The collecting anode is biased to +3 volts to reject positive ions. The bias screen changes polarity at 1 kHz, alternately allowing/rejecting dust particles with kinetic energies less than 11 V. These voltages are designed so that only charged dust particles are collected in the mesosphere (although higher energy electrons and ions are not rejected). The particle current that reaches the anode is measured by a low pass filtered DC coupled circuit. This data path, which is sensitive to both positive and negative charged particles, is called the LF channel and was the channel which provided reliable results on Hotpay 2.

Three assumptions are necessary to arrive at a charged dust particle density from the measured current: (1) all thermal electrons were rejected, (2) negative ion species were of low enough concentration to be an insignificant contribution to the measured current (which is confirmed with the plasma model in Section 4), and (3) the winter mesospheric night-time MSPs are charged negative through the attachment of only one electron (Rapp et al., 2007, Rapp and Lübken, 2001). With these assumptions, the concentration of charged MSPs as a function of altitude can be determined from the measured current I_a by the relation

$$[\text{Charged MSPs}] = \frac{I_a}{e.v_{eff}.A_{detector}} \qquad (1)$$

where v_{eff} is the effective ram velocity into the detector aperture which corrects for angle of attack and rocket coning; $A_{detector}$ is the area of the collecting anode; and e is the fundamental charge unit per particle.

This calculation can be improved by correcting for the collection efficiency and instrumental effects of the Dartmouth Dust Detector. There are 6 screens on the front of the detector. Each has an optical transmission of 90%, so the efficiency of the screens alone is ~53% (= 0.9^6). Many studies (e.g. Horanyi et al. (1999), Rapp and Thomas (2006), Hedin et al. (2007)), have shown that the function of rocket-based Faraday cups can be severely hampered by aerodynamic flows, pressure build up, and particle entrainment in and around these devices. A Monte-Carlo detector efficiency model was used to determine the instrumental collection efficiency for the specific HotPay 2 trajectory, where the payload traversed the 80 - 90 km region at the relatively high speed of 2.3 km s^{-1}. An MSP density of 2 g cm^{-3} was assumed (Saunders and Plane, 2006, Saunders and Plane, 2011). The effects of aerodynamics and heating on the incident dust flux were determined via numerical simulations. The aerodynamic environment inside the detector was calculated using the Direct Simulation Monte Carlo (DSMC) code (Bird, 1994). The DMSC code was run for a range of altitudes using the HotPay 2 trajectory and ambient atmospheric conditions determined by the MSISE-90 model (Hedin, 1991). These data were used as input to a two-dimensional model of dust particle trajectories in and around the detector. The trajectory model includes electrodynamics, atmospheric drag, particle heating and ablative mass loss in the calculation of dust particle trajectories through the detector, in the manner of Horanyi et al. (1999). Ablative mass loss was calculated using an assumed vapor pressure consistent with rock-like materials (Podolak et al., 1988).

238 The calculated dust collection efficiency is shown in Figure 3. Dust particles larger
239 than approximately 1.0 nm do not contribute to the LF current. The minimum
240 detected dust particle size decreases with altitude as the aerodynamic shocks diminish.
241 Detector efficiency decreases rapidly with altitude below about 85 km due to
242 aerodynamic effects, but average detection efficiency over the 0.5 – 1.0 nm range is
243 nearly constant at ~ 50% above 85 km. This altitude is where the peak in the
244 distribution of this size range of MSPs typically occurs (Saunders et al., 2007,
245 Bardeen et al., 2008, Megner et al., 2008); see also Section 4. Thus the total detector
246 efficiency is 50% × 53% = ~27%. The measured current from the Faraday cup is
247 therefore multiplied by a correction factor of 3.7 (= 1/0.27). This correction is applied
248 to the entire charged aerosol density profile.

249

250 The resulting profile is illustrated in Figure 4. The topside of the charged MSP profile
251 should be representative of the true geophysical charged MSP population during the
252 Hotpay 2 flight. Evidence for this is the sensible agreement with the charge non-
253 neutrality (i.e. [Ions] – [electrons]) determined from the profiles of ions and electrons
254 in Figure 2. Because the weak plasma from 70-110 km can be expected to be quasi-
255 neutral, and because the negatively-charged MSPs are too massive to be measured by
256 the Faraday rotation experiment, the difference in the measured electron and positive
257 ion concentrations should result in a profile of the negatively charged dust particles.
258 The plot of this charge imbalance in Figure 4 matches quite well that of the MSPs
259 above 85 km, indicating that a substantial fraction of the “missing” electrons reside on
260 MSPs. Note that the imbalance is greater than the measured MSPs, which is expected
261 since the Dartmouth Detector is only sensitive to particles between 0.5 and 1.0 nm.

The bottomside of the profile below 85 km is dominated by larger instrumental effects than the single point adjustment can correct for.

2.4 Na and temperature measurements by ground-based lidar

The Weber Na lidar at the ALOMAR observatory (She et al., 2006) is capable of measuring the Na density, temperature and horizontal winds in the MLT. Details of the instrument specifications and performance are provided by Dunker et al. (2013). The Na density and temperature profiles were measured by the lidar between 20:00 and 20:09 LT, immediately before the launch at 20:14 LT. The Na density profile is illustrated in Figure 1. Note the close match in height and bottom and top scale height between the Na and atomic O layers. The temperature profile is plotted in Figure 5, and compared with a typical January mean profile for this latitude, taken in this case from the SOCRATES 2D model (Khosravi et al., 2002). The measured profile shows a region of pronounced cooling between 95 and 100 km (the temperature fell to below 150 K at 100 km), which was the cool phase of a large wave with a period of 40 min (see Fig. 11 in Enell et al. (2011)).

3. Modelling

We now use three coupled models to interpret the HotPay 2 results. The overall objective was to see whether the measured absolute densities of atomic Na, positive ions and electrons, and negatively-charged MSPs can be described self-consistently – i.e., with the same meteoric ablation input rate, atomic O profile, vertical transport etc. Secondary objectives were to explore the dominant role of atomic O in

controlling the underside of the Na layer, and in partitioning electrons between negative molecular ions and MSPs.

3.1 Na layer model

Here we use a 1D time-resolved model of Na chemistry in the MLT, which extends from 65 to 110 km with 0.5 km resolution (Plane, 2004). This model treats explicitly the major sodium species – Na, $NaHCO_3$ and Na^+ - and a number of other minor species are treated implicitly using steady-state relationships. The permanent removal of sodium occurs either through dimerization of $NaHCO_3$, or attachment of sodium species to MSPs. The MSP surface area required to calculate the uptake rate was determined from the MSP model described in Section 3.2. An uptake coefficient of 0.6 was assumed (i.e. 60% of collisions between Na species and smoke particles results in permanent removal). This value implies very efficient uptake, as observed in the laboratory for the uptake of Na atoms on a silica surface (Murray and Plane, 2005). The Na chemistry is driven by the major mesospheric species O, H, H_2, CO_2, H_2O and O_3. For modelling the conditions of HotPay 2, these concentrations were calculated offline in our 1D model MESOMOD (Murray and Plane, 2005), but with the atomic O and temperature profiles constrained to the measurements (Figures 1 and 5). Outside of the height range where measurements were available, [O] and T were interpolated to the free-running MESOMOD values for January at 69^o N.

The ion-molecule chemistry of sodium dominates above 90 km, and is controlled by NO^+, O_2^+ and e^- (Plane, 2004). Since the HotPay 2 measurements show that there is charge balance between positive ions and electrons above 90 km (Figure 2), the measured values were used in the model. The positive ions were assumed to be NO^+

and O_2^+, with the NO^+ relative density varying from 19% at 85km to 91% at 100 km, in accord with the IRI 2007 model (Bilitza and Reinisch, 2008).

Vertical transport in the models used in this study was characterised by the vertical eddy diffusion coefficient, K_{zz}. In this study we have used a profile from SOCRATES (Khosravi et al., 2002) for January at 69^o N, and reduced this by a factor of 0.6. The reason for doing so is that the resulting profile of K_{zz} (Figure 5) is closer to that generated by 3D general circulation models, as discussed by Gardner et al. (2011). The average value between 80 and 90 km is 2.1×10^5 cm^2 s^{-1}, which is below the upper limit of 3×10^5 cm^2 s^{-1} required to produce the observed gravitational separation of CO_2 (Chabrillat et al., 2002). In fact, the precise choice of K_{zz} is unimportant, so long as the same profile is used in these coupled models. The input of Na, and the major components of MSPs (Fe, Mg and Si) which result from meteoric ablation, is of course sensitive to K_{zz} since faster vertical diffusive transport will need to be balanced by a larger meteoric input (Plane, 2004). The strategy in this study was to treat this input as a variable parameter, having chosen the K_{zz} profile.

3.2 Meteoric smoke particle model

A 1-D particle microphysics model (Saunders et al., 2007) was used to determine the growth and vertical distribution of MSPs. Since Fe, Mg and Si are predicted to ablate with similar efficiencies from meteoroids (Vondrak et al., 2008), we have assumed here that the MSPs are a mixture of olivines ($Fe_{2-2x}Mg_{2x}SiO_4$, $0 \le x \le 1$) and pyroxenes ($Fe_{1-x}Mg_xSiO_3$, $0 \le x \le 1$). Although in a previous study (Saunders et al., 2007) we examined the effect of magnetic dipole-driven coagulation and the likely

fractal nature of MSPs, in practice this makes little difference above 70 km compared with treating MSPs as low density spheres (Saunders et al., 2007). Here we assume that MSPs are spheres with a density of 2 g cm^{-3}.

Particle growth through coagulation is treated using a semi-implicit, volume-conserving model (Saunders and Plane, 2006). Growth occurs through a number of discrete size bins where the first bin size (r_1 = 0.25 nm) corresponds to the radius of a single monomer, which therefore has a mass of ~80 amu (since the monomer is treated as spherical). The size (r_i) of successive bins is scaled geometrically (i.e., $r_{i+1} = f^{1/3} r_i$, where f = 1.7), so that the radius of the largest of the 25 bins in the model is r_{25} = 17.4 nm.

Collisions between particles in all size bins are treated in the following way. Single gas-phase molecules are able to condense and form particles spontaneously (i.e. without a thermodynamic barrier), which we have demonstrated to be the case from the growth kinetics of Mg-Fe-SiO particles in the laboratory (Saunders and Plane, 2006, Saunders and Plane, 2011). Growth is then assumed to be dominated by Brownian diffusion-coagulation where collisions between pairs of particles result in coalescence, maintaining spherical morphology and compact structure (particle density = 2 g cm^{-3}). The collision rate coefficients (or kernels) for Brownian coagulation for these small particles are calculated using the expression for the free molecular regime (Knudsen number, $K_n >> 1$), interpolated into the transition regime for larger particles (Fuchs, 1964). Gravitational sedimentation was parameterised within the model using Stokes's Law, modified for the slip-flow regime (Jacobson, 2005). The resulting MSP size distribution as a function of altitude is illustrated in Figure 6.

3.3 Dusty plasma model

Having calculated the MSP size distribution at each 0.5 km vertical level in the model, the plasma model was then used to predict the partitioning of electrons between the gas phase, negative ions and MSPs. Formation of negative ions (Brasseur and Solomon, 1984, Smirnova et al., 1988) occurs via electron attachment to O_2:

$$O_2 + e^- (+ N_2 \text{ or } O_2) \rightarrow O_2^- \quad \text{(R1)}$$

or dissociative electron attachment to O_3:

$$O_3 + e^- \rightarrow O^- + O_2 \quad \text{(R2)}$$

However, atomic O destroys the resulting negative ions before they can further react to form more stable anions such as NO_3^- and HCO_3^-:

$$O + O_2^- \rightarrow O_3 + e^- \quad \text{(R3)}$$

$$O + O^- \rightarrow O_2 + e^- \quad \text{(R4)}$$

A simple steady-state calculation using the rate coefficients in Table 1 shows that negative ion formation is shut down in the MLT when $[O] > 1 \times 10^{10}$ cm^{-3}. However, electrons may be able to attach efficiently to MSPs, and the resulting negatively-charged particles could then be stable to charge exchange with atomic O. Since the electron affinity of O is 1.46 eV (Lide, 2006), this requires electrons to attach quite strongly to MSPs. Note that other major species have much smaller electron affinities (e.g. 0.43 eV for O_2) and although the electron affinity of O_3 is 2.1 eV (Lide, 2006), the concentration of O_3 is two orders of magnitude smaller than O above 80 km.

In order to explore both the kinetics of electron attachment and the electron binding energies, we carried out a series of electronic structure calculations on the relevant

pyroxene and olivine monomers and small clusters. The hybrid density functional / Hartree-Fock B3LYP method was employed from within the Gaussian 09 suite of programs (Frisch et al., 2009), combined with the 6-311+G(2d,p) triple zeta basis set. This is a large, flexible basis set which has both polarization and diffuse functions added to the atoms. At this level of theory, the expected uncertainty in the calculated reaction enthalpies is ±0.2 eV (Foresman and Frisch, 1996). Molecular geometries were first optimised and checked for wavefunction stability. Figure 7 illustrates examples of MSPs which have a sphere-equivalent radius of about 0.4 nm.

The resulting electron attachments energies are listed in Table 2. Note that for molecules containing one or more Fe atoms, several electronic spin multiplicities are possible in both the neutral and anionic forms. The lowest energy spin states were therefore determined and used to compute the electron attachment energies. These spin states are listed in Table 2. In the case of all the embryonic MSPs containing Si (i.e. the olivines and pyroxenes), the electron affinities are larger than that of O (several by more than 1eV), and so they should form rapidly (see below) and be stable to charge exchange with O. In contrast, the metal hydroxides have relatively low electron attachment energies.

The rate coefficient for electron attachment to $FeMgSiO_4$ (as a representative example) was calculated using Rice-Ramsperger-Kassel-Markus (RRKM) theory with a solution of the Master Equation based on the inverse Laplace transform method (De Avillez Pereira et al., 1997). We have applied this formalism previously to recombination reactions of metallic species (Vondrak et al., 2006, Broadley et al., 2007, Plane, 2013), so only a brief description is given here. Electron attachment proceeds via the formation of an excited adduct anion, which can either dissociate again or be stabilized by collision with a so-called third body (N_2 or O_2 in the MLT).

406 The internal energy of this adduct was divided into a contiguous set of grains (width
407 30 cm^{-1}), each containing a bundle of rovibrational states. Each grain was then
408 assigned a set of microcanonical rate coefficients for dissociation, which were
409 determined using inverse Laplace transformation to link them directly to the electron-
410 molecule capture rate coefficient estimated from Langevin theory:

$$k_L = 2\pi e\sqrt{\frac{\alpha_v}{4\pi\varepsilon_0\mu}} \quad (2)$$

412

413 where α_v is the volume polarizability of olivine (Table 3), e is the electronic charge,
414 and μ is the reduced mass of the e^- - olivine collision pair. k_L increases by only 8% at
415 200 K if a correction for s-wave scattering is included (Troe et al., 2007).

416 The density of states of the adduct was calculated using the Beyer-Swinehart
417 algorithm for the vibrational modes (without making a correction for anharmonicity),
418 and a classical densities of states treatment for the rotational modes (Gilbert and
419 Smith, 1990). The vibrational frequencies and rotational constants for $FeMgSiO_4$ and
420 its ion, calculated from the electronic structure calculations described above, are listed
421 in Table 3. The e^--olivine adduct has a high density of rovibrational states because of
422 the large binding energy and number of low frequency vibrational modes. Thus, the
423 electron attachment is essentially at the high-pressure limit over the pressure range of
424 the MLT. The resulting capture rate coefficient is 4.1×10^{-7} $(200 / T)^{0.21}$ cm^3
425 $molecule^{-1}$ s^{-1}. This rate coefficient is similar to that for electron attachment to SF_6
426 (Troe et al., 2007). In contrast, electron attachment to O_2, where the binding energy is
427 only 0.43 eV and there is a single vibrational mode, is very slow and pressure
428 dependent (Table 1), being around 3×10^{-17} cm^3 $molecule^{-1}$ s^{-1} at 80 km. The

429 calculated rate of electron capture to $FeMgSiO_4$ confirms that this process should be
430 relatively fast for even the smallest MSPs.

431 The dusty plasma model was constructed with three MSP size bins: (1) $0.25 \leq r < 0.5$
432 nm, corresponding to masses between 130 and 390 amu; (2) $0.5 \leq r < 1.0$ nm,
433 corresponding to masses between 390 and 5600 amu; (3) and larger/heavier particles.
434 The size distributions between 75 and 95 km from the 1D MSP growth model
435 (Section 3.2, Figure 6) were used to fill each of the bins with MSPs in the appropriate
436 size range, and also to calculate a weighted average radius for each bin: 0.35 nm for
437 bin 1; 0.69 nm for bin 2; and 2.25 nm for bin 3. Bin 2 corresponds to the size/mass
438 range measured by the Dartmouth Dust Detector.

439 The charging of the MSPs in the weak plasma of the MLT region was then described
440 by the standard Natanson expressions (Natanson, 1960, Jensen and Thomas, 1991),
441 which are listed in Table 1. It is interesting to compare the rate coefficient for electron
442 attachment to a small MSP (r = 0.25 nm) calculated using the Natanson expression,
443 which gives a rate coefficient of 4.1×10^{-7} cm^3 $molecule^{-1}$ s^{-1} at 200K, with the
444 Langevin/RRKM result discussed above – the agreement is excellent. The rate
445 coefficients for electron attachment to neutral MSPs are multiplied by a factor η (≤ 1)
446 in the model. The reason for doing this is discussed below in Section 4.

447 The final part of the plasma model is the rate of ion-pair production, q, and the rate
448 coefficient for dissociative recombination of positive ions with electrons, k_{DR}. The
449 latter is assigned a value of 3×10^{-7} cm^3 $molecule^{-1}$ s^{-1}, typical of the rate coefficients
450 for a wide range of small positive ions (Florescu-Mitchell and Mitchell, 2006).
451 Following previous practice (Jensen and Thomas, 1991), we assume that the rates of
452 ion-pair production and dissociative recombination are balanced:

$$q = k_{DR} (I^+)^2 \quad (3)$$

This expression should hold above 90 km, where electrons are essentially all in the gas phase and equal in concentration to the positive ions (Figure 2). At lower altitudes where the electrons are attached to molecules or particles and the rate of recombination of these species with positive ions is slower, equation 3 probably overestimates q. Application of equation to the positive ion profile in Figure 2 yields a profile for q with height that is nearly exponential: $\ln(q / cm^{-3} s^{-1}) = 33.2 - 1.08z + 7.92 \times 10^{-3} z^2$.

4. Discussion

Figure 1 shows the close relationship between atomic O and Na in the MLT. This is the first time that near-coincident measurements of these species have been made: the payload and lidar were separated by only 2.58 km at 90 km altitude and the Na density measurements were made between 5 and 14 min before the rocket launch. This constitutes a significant improvement on an earlier rocket-lidar experiment in northern Brazil in 1995, where the rocket payload passed through the Na layer about 40 km from a zenith-pointing lidar which had to average for more than an hour to obtain sufficient signal-to-noise in the retrieved Na layer (Clemesha et al., 1995). Atomic O controls the underside of the Na layer directly by reducing the oxides back to Na (Helmer and Plane, 1993, Plane, 2003, Plane, 2004):

$$NaO + O \rightarrow Na + O_2 \quad (R5)$$

$$NaO_2 + O \rightarrow NaO + O_2 \quad (R6)$$

$$NaO_3 + O \rightarrow NaO_2 + O_2 \quad (R7)$$

Moreover, atomic O exercises an indirect control because it determines the atomic H profile (Plane, 2003), and H converts the stable Na reservoir $NaHCO_3$ back to Na (Cox et al., 2001):

$$NaHCO_3 + H \rightarrow Na + H_2CO_3 \qquad (R8)$$

The 1D model described in Section 3.1, constrained by the measured atomic O and temperature profiles, was now used to determine the Na ablation flux required to model the observed Na layer. This was 8400 Na atom cm^{-2} s^{-1}, which is equivalent to a global meteoric mass input rate of ~20 t d^{-1} (Vondrak et al., 2008). It should be noted that the actual meteoric mass input rate is highly uncertain (Plane, 2012). From a modelling point of view, the required input rate correlates with K_{zz} (Plane, 2004, Feng et al., 2013), itself a simplistic parameterization of turbulent diffusion caused by gravity wave breaking.

Figure 8 shows the diurnal Na layer profile for January, 69^o N. Note the increase of Na on the underside of the layer resulting from the photolysis of the reservoir $NaHCO_3$ and increase of atomic H (enhancing reaction R8), during the few hours of daylight around local noon. The accompanying daytime decrease of Na on the topside of the layer is caused by photo-ionization and charge transfer with ambient NO^+ and O_2^+ ions (Plane, 2004). The time of the HotPay 2 launch is indicated on the figure. Figure 9 shows the Na density profile at that time, along with the lidar measurement. There is clearly excellent agreement, not so much in the absolute density (since the Na injection rate from ablation is an optimised parameter in the model), but in capturing the peak height and bottom- and top-side scale heights of the layer. Also shown in Figure 9 are the major Na reservoirs, Na^+ ions above the layer and $NaHCO_3$ below.

Fe, Mg and Si ablate from meteoroids less efficiently than Na (Vondrak et al., 2008). For example, in a study of Fe and Na layer observations at South Pole (Gardner et al., 2005), and in a recent study of the global Fe layer (Feng et al., 2013), the Fe meteoric input flux needed to be reduced by a factor of ~4, so that the Fe:Na injection rate was 4:1, compared with a chondritic ratio of 16:1. Since Mg and Si ablate with similar efficiencies to Fe (Vondrak et al., 2008), we assume a source of olivine MSP particles (r_1 = 0.25 nm) of 5 t d^{-1} i.e. equivalent to 25% of the meteoric mass input rate required to model the Na layer.

Figure 6 shows that above 70 km most of the MSPs are predicted to be in the size range below 1 nm, with a maximum number density of 25,500 particles cm^{-3} at 77 km. The number density of even these very small particles falls off rapidly above 85 km because sedimentation competes effectively with upward mixing by turbulent diffusion. These particle densities and vertical profiles are in sensible accord with measurements (e.g. Rapp et al. (2007), Robertson et al. (2013)) and previous models (e.g. Megner et al. (2008), Bardeen et al. (2008), Saunders et al. (2012)).

Inspection of Table 2 shows that all the candidate olivine and pyroxene species (up to the trimers in the case of the latter) have substantial electron attachment energies, which are mostly significantly higher than the electron affinity of O (1.46 eV). In contrast, the electron attachment energies to the Fe and Mg hydroxide species are less than 1.4 eV, which means that the electron attachment rates will be significantly lower, and they will be liable to charge transfer with atomic O (where the concentration of O is significant above 80 km). Since small MSPs contain only two or three Mg, Fe or Si oxide subunits (Figure 7), a fraction of them will not contain any silicon and thus not attach electrons efficiently in the MLT when atomic O is present. Furthermore, an electron may not always attach depending on the part of the particle

526 with which it collides: the positively-charged metal atoms being more attractive than
527 the negatively-charged O atoms e.g. in $FeMgSiO_4$, the Mulliken charges on the Fe,
528 Mg and Si atoms are +0.7, +0.9 and +2.0, respectively, whereas the O atoms all carry
529 a charge of -0.9. To take these two factors into account, we have multiplied the rate
530 coefficients for e^- attachment to neutral MSPs in the three size bins by a factor of η. A
531 value for η of 0.5 produces the vertical profile of negatively-charged MSP2 particles
532 (i.e. in bin 2, corresponding to r between 0.5 and 1.0 nm) shown in Figure 4, which is
533 a good fit to the profile of negatively-charged particles measured by the Dartmouth
534 Dust Detector above 85 km - both in terms of the absolute numbers of particles and
535 fall-off with altitude. Below 85 km the pressure is too high for the single point
536 correction applied to the raw detector data to be reliable (Section 2.3). If η is set to 1,
537 then the peak density of MSP^- particles increases to 440 cm^{-3} at 85.5 km, which is still
538 within the uncertainty of the measurements.

539 Figure 2 shows a comparison of the modelled and measured profiles of positive ions
540 and electrons from 75 to 105 km. The model captures well the marked charge
541 imbalance below 90 km, where the electron depletion increases to nearly 2 orders of
542 magnitude by 75 km. Most of this is due to the negative charging of MSPs, although
543 Figure 2 shows that negative ions start to become significant below 80 km when [O]
544 falls below 10^{10} cm^{-3}.

545 Figure 10 illustrates the charge state of MSPs in the three size bins. The majority of
546 particles are MSP1 (i.e. in bin 1) at all heights above 75 km (although close to 75 km
547 the MSP1 and MSP2 populations are starting to decrease relative to MSP3 due to
548 coagulation). Most MSPs carry a single negative charge above 87 km, whereas below
549 this the particles are more likely to be neutral. Note that positive particles start to
550 appear below 85 km, because highly-mobile free electrons have essentially all been

551 removed, either forming negative MSPs or molecular anions. Positive particles are
552 then neutralised by much slower collisions with these species. In fact, positive MSPs
553 have recently been observed below 80 km for the first time (Robertson et al., 2013).
554

555 Conclusions

556 This paper describes the results from a successful rocket experiment where the
557 measurement of atomic O, negatively-charged dust, positive ions and electrons on the
558 payload was complemented by lidar measurements of atomic Na and temperature
559 from the ground. There are two significant conclusions. First, it has been possible to
560 model the atomic Na layer, and the vertical profiles of negatively-charged MSPs,
561 electrons and positive ions, using a self-consistent meteoric input flux. Second, we
562 have used electronic structure calculations and RRKM theory to show that even the
563 smallest MSPs are able to attach electrons very rapidly compared with electron
564 attachment to O_2 and O_3, and form stable negatively-charged particles, if they contain
565 silicon. This explains why substantial electron depletions can occur above 80 km,
566 where the presence of atomic O prevents the formation of stable negative ions.
567

568 Acknowledgments

569 The HotPay 2 rocket experiment was supported by the EU's 6th Framework Program
570 under the project "ALOMAR eARI", contract no. RITA-CT-2003-506208, and a
571 grant from the Royal Society. The theory and modelling work was supported by
572 project number 291332 (CODITA – Cosmic Dust in the Terrestrial Atmosphere) from
573 the European Research Council. The ALOMAR Na lidar was supported by grants
574 AGS-1136269 and AGS-0545262 from the National Science Foundation.

References

Bardeen, C.G., Toon, O.B., Jensen, E.J., Marsh, D.R., Harvey, V.L., 2008. Numerical simulations of the three-dimensional distribution of meteoric dust in the mesosphere and upper stratosphere. J. Geophys. Res. 113 (D17), art. no.: D17202.

Bennett, F.D.G., Hall, J.E., Dickinson, P.H.G., 1972. D-Region Electron Densities and Collision Frequencies from Faraday Rotation and Differential Absorption. J. Atmos. Terr. Phys. 34, 1321-1335.

Bilitza, D., Reinisch, B.W., 2008. International Reference Ionosphere 2007: Improvements and new parameters. Adv. Space Res. 42 (4), 599-609.

Bird, G.A., 1994. Molecular gas dynamics and the direct simulation of gas flows. Oxford University Press.

Blix, T.A., Thrane, E.V., Fritts, D.C., von Zahn, U., Lubken, F.J., Hillert, W., Blood, S.P., Mitchell, J.D., Kokin, G.A., Pakhomov, S.V., 1990. Small-scale structure observed in situ during MAC EPSILON. J. Atmos. Solar-Terr. Phys. 52 (10-11), 835-854.

Brasseur, G., Solomon, S., 1984. Aeronomy of the Middle Atmosphere. D. Reidel Publishing Company.

Broadley, S.L., Vondrak, T., Plane, J.M.C., 2007. A kinetic study of the reactions of Ca^+ ions with O_3, O_2, N_2, CO_2 and H_2O. Phys. Chem. Chem. Phys. 9 (31), 4357-4369.

Chabrillat, S., Kockarts, G., Fonteyn, D., Brasseur, G., 2002. Impact of molecular diffusion on the CO_2 distribution and the temperature in the mesosphere. Geophys. Res. Lett. 29 (15), art. no.: 1729

Clemesha, B.R., Simonich, D.M., Takahashi, H., Melo, S.M.L., Plane, J.M.C., 1995. Experimental evidence for photochemical control of the atmospheric sodium layer. J. Geophys. Res. 100 (D9), 18909-18916.

Cox, R.M., Self, D.E., Plane, J.M.C., 2001. A study of the reaction between $NaHCO_3$ and H: Apparent closure on the chemistry of mesospheric Na. J. Geophys. Res. 106 (D2), 1733-1739.

De Avillez Pereira, R., Baulch, D.L., Pilling, M.J., Robertson, S.H., Zeng, G., 1997. J. Phys. Chem. 101, 9681.

Dunker, T., Hoppe, U.P., Stober, G., Rapp, M., 2013. Development of the mesospheric Na layer at 69 degrees N during the Geminids meteor shower 2010. Ann. Geophys. 31 (1), 61-73.

Enell, C.-F., Hedin, J., Stegman, J., Witt, G., Friedrich, M., Singer, W., Baumgarten, G., Kaifler, B., Hoppe, U.-P., Gustavsson, B., Brandstrom, U., Khaplanov, M., Kero, A., Ulich, T., Turunen, E., 2011. The Hotel Payload 2 campaign: Overview of NO, O and electron density measurements in the upper mesosphere and lower thermosphere. J. Atmos. Solar-Terr. Phys. 73 (14-15), 2228-2236.

Feng, W., Marsh, D.R., Janches, D., Hoeffner, J., Yi, F., Chipperfield, M.P., Plane, J.M.C., 2013. A global atmospheric model of meteoric iron. J. Geophys. Res. 118, 9456–9474.

Fentzke, J.T., Janches, D., Strelnikova, I., Rapp, M., 2009. Meteoric smoke particle properties derived using dual-beam Arecibo UHF observations of D-region spectra during different seasons. J. Atmos. Solar-Terr. Phys. 71 (17-18), 1982-1991.

Florescu-Mitchell, A.I., Mitchell, J.B.A., 2006. Dissociative recombination. Phys. Rep. 430 (5-6), 277-374.

Foresman, J.B., Frisch, A., 1996. Exploring chemistry with electronic structure methods. Gaussian, Inc.

Friedrich, M., Rapp, M., Blix, T., Hoppe, U.P., Torkar, K., Robertson, S., Dickson, S., Lynch, K., 2012. Electron loss and meteoric dust in the mesosphere. Annal. Geophys. 30 (10), 1495-1501.

Friedrich, M., Rapp, M., Plane, J.M.C., Torkar, K.M., 2011. Bite-outs and other depletions of mesospheric electrons. J. Atmos. Solar-Terr. Phys. 73 (14-15), 2201-2211.

Frisch, M.J., Trucks, G.W., Schlegel, H.B., Scuseria, G.E., Robb, M.A., Cheeseman, J.R., Scalmani, G., Barone, V., Mennucci, B., Petersson, G.A., Nakatsuji, H., Caricato, M., Li, X., Hratchian, H.P., Izmaylov, A.F., Bloino, J., Zheng, G., Sonnenberg, J.L., Hada, M., Ehara, M., Toyota, K., Fukuda, R., Hasegawa, J., Ishida, M., Nakajima, T., Honda, Y., Kitao, O., Nakai, H., Vreven, T., J. A. Montgomery, J., Peralta, J.E., Ogliaro, F., Bearpark, M., Heyd, J.J., Brothers, E., Kudin, K.N., Staroverov, V.N., Kobayashi, R., Normand, J., Raghavachari, K., Rendell, A., Burant, J.C., Iyengar, S.S., Tomasi, J., Cossi, M., Rega, N., Millam, J.M., Klene, M., Knox, J.E., Cross, J.B., Bakken, V., Adamo, C., Jaramillo, J., Gomperts, R., Stratmann, R.E., Yazyev, O., Austin, A.J., Cammi, R., Pomelli, C., Ochterski, J.W., Martin, R.L.,

642 Morokuma, K., Zakrzewski, V.G., Voth, G.A., Salvador, P., Dannenberg, J.J.,
643 Dapprich, S., Daniels, A.D., Farkas, O., Foresman, J.B., Ortiz, J.V., Cioslowski, J.,
644 Fox, D.J., 2009. Gaussian 09, Revision A.1. Gaussian, Inc.

645 Fuchs, N.A., 1964. Mechanics of Aerosols. Pergamon.

646 Gardner, C.S., Chu, X., Espy, P.J., Plane, J.M.C., Marsh, D.R., Janches, D., 2011.
647 Seasonal variations of the mesospheric Fe layer at Rothera, Antarctica (67.5°S,
648 68.0°W). J. Geophys. Res. 116, article number: D02304,
649 doi:02310.01029/02010JD014655.

650 Gardner, C.S., Plane, J.M.C., Pan, W.L., Vondrak, T., Murray, B.J., Chu, X.Z., 2005.
651 Seasonal variations of the Na and Fe layers at the South Pole and their implications
652 for the chemistry and general circulation of the polar mesosphere. J. Geophys. Res.
653 110 (D10), art. no. D10302.

654 Gelinas, L.J., Lynch, K.A., Kelley, M.C., Collins, R.L., Widholm, M., MacDonald,
655 E., Ulwick, J., Mace, P., 2005. Mesospheric charged dust layer: Implications for
656 neutral chemistry. J. Geophys. Res. 110 (A1), art. no.: A01310.

657 Gilbert, R.G., Smith, S.C., 1990. Theory of Unimolecular and Recombination
658 Reactions. Blackwell.

659 Greer, R.G.H., Murtagh, D.P., McDade, I.C., Dickinson, P.H.G., Thomas, L., Jenkins,
660 D.B., Stegman, J., Llewellyn, E.J., Witt, G., Mackinnon, D.J., Williams, E.R., 1986.
661 ETON-1 - a database pertinent to the study of energy-transfer in the oxygen
662 nightglow. Planet. Space Sci. 34 (9), 771-788.

663 Hedin, A.E., 1991. Extension of the MSIS Thermospheric Model into the Middle and
664 Lower Atmosphere. J. Geophys. Res. 96, 1159-1172.

665 Hedin, J., Gumbel, J., Rapp, M., 2007. On the efficiency of rocket-borne particle
666 detection in the mesosphere. Atmos. Chem. Phys. 7, 3701-3711.

667 Hedin, J., Gumbel, J., Stegman, J., Witt, G., 2009. Use of O_2 airglow for calibrating
668 direct atomic oxygen measurements from sounding rockets. Atmos. Meas. Tech. 2
669 (2), 801-812.

670 Helmer, M., Plane, J.M.C., 1993. A Study of the Reaction $NaO_2 + O \rightarrow NaO+O_2$ -
671 Implications for the Chemistry of Sodium in the Upper Atmosphere. J. Geophys. Res.
672 98 (D12), 23207-23222.

673 Hervig, M.E., Gordley, L.L., Deaver, L.E., Siskind, D.E., Stevens, M.H., Russell,
674 J.M., Bailey, S.M., Megner, L., Bardeen, C.G., 2009. First Satellite Observations of
675 Meteoric Smoke in the Middle Atmosphere. Geophys. Res. Lett. 36, art. no:L18805.

676 Horanyi, M., J., Gumbel, G., Witt, Robertson, S., 1999. Simulation of rocket-borne
677 particle measurements in the mesosphere. Geophys. Res. Lett. 26, 1537–1540.

678 Hunten, D.M., Turco, R.P., Toon, O.B., 1980. Smoke and dust particles of meteoric
679 origin in the mesosphere and stratosphere. J. Atm. Sci. 37 (6), 1342-1357.

680 Jacobsen, T.A., Friedrich, M., 1979. Electron density measurements in the lower D-
681 region. J. Atmos.Terr. Phys. 41 (12), 1195-1200.

682 Jacobson, M.Z., 2005. Fundamentals of Atmospheric Modeling. Cambridge
683 University Press.

684 Jensen, E.J., Thomas, G.E., 1991. Charging of mesospheric particles - implications for
685 electron-density and particle coagulation. J. Geophys. Res. 96 (D10), 18603-18615.

686 Khosravi, R., Brasseur, G., Smith, A., Rusch, D., Walters, S., Chabrillat, S., Kockarts,
687 G., 2002. Response of the mesosphere to human-induced perturbations and solar
688 variability calculated by a 2-D model. J. Geophys. Res. 107 (D18).

689 Lide, D.R., 2006. Handbook of Physics and Chemistry. CRC Press.

690 Lynch, K.A., Gelinas, L.J., Kelley, M.C., Collins, R.L., Widholm, M., Rau, D.,
691 MacDonald, E., Liu, Y., Ulwick, J., Mace, P., 2005. Multiple sounding rocket
692 observations of charged dust in the polar winter mesosphere. J. Geophys. Res. 110
693 (A3), Article Number: A03302 DOI: 03310.01029/03200JA010502.

694 Megner, L., Siskind, D.E., Rapp, M., Gumbel, J., 2008. Global and temporal
695 distribution of meteoric smoke: A two-dimensional simulation study. J. Geophys. Res.
696 113 (D3), art. no.: D03202.

697 Murray, B.J., Plane, J.M.C., 2005. Modelling the impact of noctilucent cloud
698 formation on atomic oxygen and other minor constituents of the summer mesosphere.
699 Atm. Chem. Phys. 5, 1027-1038.

700 Murray, B.J., Plane, J.M.C., 2005. Uptake of Fe, Na and K atoms on low-temperature
701 ice: implications for metal atom scavenging in the vicinity of polar mesospheric
702 clouds. Phys. Chem. Chem. Phys. 7 (23), 3970-3979.

703 Murtagh, D.P., 1989. A self-consistent model of the most common nightglow
704 emissions. In: Burke, W.R. (Ed.), Proceedings of the Ninth ESA/PAC Symposium on

European Rocket and Balloon Programmes and related research (ESA SP-291). 167–171. European Space Agency.

Natanson, G.L., 1960. On the theory of the charging of microscopic aerosol particles as a result of capture of gas ions. Soviet Phy. -Techn. Phys. 5 (5), 538-551.

Plane, J.M.C., 2003. Atmospheric chemistry of meteoric metals. Chem. Rev. 103 (12), 4963-4984.

Plane, J.M.C., 2004. A time-resolved model of the mesospheric Na layer: constraints on the meteor input function. Atmos. Chem. Phys. 4, 627-638.

Plane, J.M.C., 2012. Cosmic dust in the earth's atmosphere. Chem. Soc. Rev. 41 (19), 6507-6518.

Plane, J.M.C., 2013. On the nucleation of dust in oxygen-rich stellar outflows. Phil. Trans. R. Soc. A 371, art. no. 20120335.

Podolak, M., Pollack, J.B., Reynolds, R.T., 1988. Interactions of planetesimals with protoplanetary atmospheres. Icaraus 73, 163-179.

Rapp, M., Lübken, F.J., 2001. Modeling of particle charging in the polar summer mesosphere: Part 1 – general results. J. Atmos. Solar-Terr. Phys. 63, 759–770.

Rapp, M., Plane, J.M.C., Strelnikov, B., Stober, G., Ernst, S., Hedin, J., Friedrich, M., Hoppe, U.P., 2012. In situ observations of meteor smoke particles (MSP) during the Geminids 2010: constraints on MSP size, work function and composition. Annal. Geophys. 30 (12), 1661-1673.

725 Rapp, M., Strelnikova, I., Gumbel, J., 2007. Meteoric smoke particles: Evidence from
726 rocket and radar techniques. Adv. Space Res. 40 (6), 809-817.

727 Rapp, M., Strelnikova, I., Gumbel, J., 2007. Meteoric smoke particles: evidence from
728 rocket and radar techniques. Adv. Space Res. 40, 809-817.

729 Rapp, M., Strelnikova, I., Strelnikov, B., Hoffmann, P., Friedrich, M., Gumbel, J.,
730 Megner, L., Hoppe, U.P., Robertson, S., Knappmiller, S., Wolff, M., Marsh, D.R.,
731 2010. Rocket-borne in situ measurements of meteor smoke: Charging properties and
732 implications for seasonal variation. J. Geophys. Res. 115, art. no: D00I16.

733 Rapp, M., Thomas, G.E., 2006. Modeling the microphysics of mesospheric ice
734 particles – assessment of current capabilities and basic sensitivities. J. Atmos. Solar-
735 Terr. Phys. 68, 715–744.

736 Robertson, S., Dickson, S., Horanyi, M., Sternovsky, Z., Friedrich, M., Janches, D.,
737 Megner, L., Williams, B.P., 2013. Detection of Meteoric Smoke Particles in the
738 Mesosphere by a Rocket-borne Mass Spectrometer. J. Atmos. Solar-Terr. Phys.
739 submitted to the special issue on mesospheric smoke and ice.

740 Rosinski, J., Snow, R.H., 1961. Secondary particulate matter from meteor vapors. J.
741 Meteorol. 18 (6), 736-745.

742 Sagalyn, R.C., Smiddy, M., 1963. Measurement and interpretation of ion density
743 distributions in daytime F region. J. Geophys. Res. 68 (1), 199-211.

744 Saunders, R.W., Dhomse, S., Tian, W.S., Chipperfield, M.P., Plane, J.M.C., 2012.
745 Interactions of meteoric smoke particles with sulphuric acid in the Earth's
746 stratosphere. Atmos. Chem. Phys. 12 (10), 4387-4398.

747 Saunders, R.W., Forster, P.M., Plane, J.M.C., 2007. Potential climatic effects of
748 meteoric smoke in the Earth's paleo-atmosphere. Geophys. Res. Lett. 34 (16), art. no.:
749 L16801.

750 Saunders, R.W., Plane, J.M.C., 2006. A laboratory study of meteor smoke analogues:
751 Composition, optical properties and growth kinetics. J. Atmos. Solar-Terr. Phys. 68
752 (18), 2182-2202.

753 Saunders, R.W., Plane, J.M.C., 2011. A Photo-Chemical Method for the Production
754 of Olivine Nanoparticles as Cosmic Dust Analogues. Icarus 212, 373-382.

755 She, C.Y., Williams, B.P., Hoffmann, P., Latteck, R., Baumgarten, G., Vance, J.D.,
756 Fiedler, J., Acott, P., Fritts, D.C., Lubken, F.J., 2006. Simultaneous observation of
757 sodium atoms, NLC and PMSE in the summer mesopause region above ALOMAR,
758 Norway (69^{o} N, 12^{o} E). J. Atmos. Solar-Terr. Phys. 68 (1), 93-101.

759 Smirnova, N.V., Ogloblina, O.F., Vlaskov, V.A., 1988. Modeling of the lower
760 ionosphere. Pure Appl. Geophys. 127 (2-3), 353-379.

761 Troe, J., Miller, T.M., Viggiano, A.A., 2007. Low-energy electron attachment to SF_6.
762 I. Kinetic modeling of nondissociative attachment. J. Chem. Phys. 127, article
763 number: 244303.

764 Vondrak, T., Plane, J.M.C., Broadley, S., Janches, D., 2008. A chemical model of
765 meteoric ablation. Atmos. Chem. Phys. 8 (23), 7015-7031.

766 Vondrak, T., Woodcock, K.R.I., Plane, J.M.C., 2006. A kinetic study of the reactions
767 of Fe^{+} with N_2O, N_2, O_2, CO_2 and H_2O, and the ligand-switching reactions $Fe^{+}.X + Y$

--> $Fe^{+}.Y + X$ ($X = N_2, O_2, CO_2$; $Y=O_2, H_2O$). Phys. Chem. Chem. Phys. 8 (4), 503-512.

775 **Table 1.** Rate coefficients in the dusty plasma model

Reaction	Rate coefficient [a]	Source
$I^+ + e^-$ production	$q = k_{DR}\ [I^+]^2$	See text
$e^- + O_2 + O_2 \rightarrow O_2^- + O_2$	$1.4\times 10^{-29}\,(300/T)\,\exp(-600/T)$	[b]
$e^- + O_2 + N_2 \rightarrow O_2^- + N_2$	1.0×10^{-31}	[b]
$e^- + O_3 \rightarrow O^- + O_2$	$9.1 \times 10^{-12}\,(300/T)^{-1.46}$	[b]
$O + O_2^- \rightarrow O_3 + e^-$	1.5×10^{-10}	[b]
$O + O^- \rightarrow O_2 + e^-$	1.9×10^{-10}	[b]
$I^+ + e^- \rightarrow$ products	$k_{DR} = 3 \times 10^{-7}$	[c]
$e^- + MSP \rightarrow MSP^-$	$\eta\pi r_{MSP}^2\sqrt{\frac{8k_BT}{\pi m_e}}\left(1+\sqrt{\frac{e^2}{8\varepsilon_0 r_{MSP}k_BT}}\right)$	[d,e]
$I^+ + MSP \rightarrow MSP^+ + I$	$\pi r_{MSP}^2\sqrt{\frac{8k_BT}{\pi m_{I^+}}}\left(1+\sqrt{\frac{e^2}{8\varepsilon_0 r_{MSP}k_BT}}\right)$	[d]
$I^- + MSP \rightarrow MSP^- + I$	$\pi r_{MSP}^2\sqrt{\frac{8k_BT}{\pi m_{I^-}}}\left(1+\sqrt{\frac{e^2}{8\varepsilon_0 r_{MSP}k_BT}}\right)$	[d]
$e^- + MSP^+ \rightarrow MSP$	$\pi r_{MSP}^2\sqrt{\frac{8k_BT}{\pi m_e}}\left(1+\frac{e^2}{4\pi\varepsilon_0 r_{MSP}k_BT}\right)$	[d]
$I^+ + MSP^- \rightarrow MSP + I$	$\pi r_{MSP}^2\sqrt{\frac{8k_BT}{\pi m_{I^+}}}\left(1+\frac{e^2}{4\pi\varepsilon_0 r_{MSP}k_BT}\right)$	[d]
$I^+ + MSP^{2-} \rightarrow MSP^- + I$	$\pi r_{MSP}^2\sqrt{\frac{8k_BT}{\pi m_{I^+}}}\left(1+\frac{2e^2}{4\pi\varepsilon_0 r_{MSP}k_BT}\right)$	[d]
$I^- + MSP^+ \rightarrow MSP + I$	$\pi r_{MSP}^2\sqrt{\frac{8k_BT}{\pi m_{I^-}}}\left(1+\frac{e^2}{4\pi\varepsilon_0 r_{MSP}k_BT}\right)$	[d]
$e^- + MSP^- \rightarrow MSP^{2-}$	$\pi r_{MSP}^2\sqrt{\frac{8k_BT}{\pi m_{e^-}}}.$ $.g^2\exp\left(\left(\frac{-e^2}{4\pi\varepsilon_0 r_{MSP}k_BT}\right)\left(1-\frac{1}{2g(g^2-1)}\right)\right)$ $g = 1.62$	[d]

776 [a] Bimolecular reactions: cm^3 $molecule^{-1}$ s^{-1}; termolecular reactions: cm^6 $molecule^{-2}$ s^{-1}.
777 [b] Florescu-Mitchell and Mitchell (2006). [c] Smirnova et al. (1988). [d] Natanson (1960),
778 Jensen and Thomas (1991). [e] The factor η (=0.5 in the plasma model) allows for
779 collisions with MSPs with electron attachment energies below 1.5 eV (see text).

780 **Table 2.** Electron attachment energies to small MSPs, calculated at the B3LYP/6-
781 311+g(2d,p) level of theory.[a] These should be compared with the electron affinity of
782 atomic O, which is1.46 eV (Lide, 2006). The number in parenthesis after each species
783 is the electronic spin multiplicity (= 2S + 1, where S is the total spin quantum
784 number).

Neutral	Anion	Electron attachment energy / eV
Olivines		
Mg_2SiO_4 (1)	$Mg_2SiO_4^-$ (2)	1.98
Fe_2SiO_4 (9)	$Fe_2SiO_4^-$ (10)	1.96
$FeMgSiO_4$ (5)	$FeMgSiO_4^-$ (6)	2.08
$[Mg_2SiO_4]_2$ (1)	$[Mg_2SiO_4]_2^-$ (2)	2.65
$[Fe_2SiO_4]_2$ (17)	$[Fe_2SiO_4]_2^-$ (18)	2.59
$[FeMgSiO_4]_2$ (9)	$[FeMgSiO_4]_2^-$ (10)	2.69
Pyroxenes		
$MgSiO_3$ (1)	$MgSiO_3$ (1)	2.79
$FeSiO_3$ (5)	$FeSiO_3$ (5)	2.59
$[MgSiO_3]_2$ (1)	$[MgSiO_3]_2$ (1)	1.59
$[FeSiO_3]_2$ (9)	$[FeSiO_3]_2$ (10)	1.96
$MgSiO_3$-$FeSiO_3$ (5)	$MgSiO_3$-$FeSiO_3$ (5)	1.96
$[FeSiO_3]_3$ (13)	$[FeSiO_3]_3^-$ (12)	2.51
$[MgSiO_3]_3$ (1)	$[MgSiO_3]_3^-$ (2)	2.83
Metal hydroxides		
FeOH (4)	$FeOH^-$ (3)	0.42
MgOH (2)	$MgOH^-$ (1)	1.18
$[FeOH]_2$ (9)	$[FeOH]_2^-$ (8)	0.97
$[MgOH]_2$ (1)	$[MgOH]_2^-$ (2)	1.19
$[FeOH]_3$ (10)	$[FeOH]_3^-$ (9)	0.31
$[MgOH]_3$ (2)	$[MgOH]_3^-$ (3)	1.56
$Fe(OH)_2$ (5)	$Fe(OH)_2^-$ (4)	1.18
$Mg(OH)_2$ (1)	$Mg(OH)_2^-$ (2)	0.23
$[Fe(OH)_2]_2$ (9)	$[Fe(OH)_2]_2^-$ (8)	0.64
$[Mg(OH)_2]_2$ (1)	$[Mg(OH)_2]_2^-$ (2)	0.32

785 [a] Zero-point energies are not included, but this should not lead to an error of more
786 than 0.1 eV.

787

788 **Table 3.** Molecular parameters for $FeMgSiO_4$ and $FeMgSiO_4^-$, calculated at the
789 B3LYP/6-311+G(2d,p) level of theory.

Species	Dipole Moment [a]	Polarizability [b]	Rotational constants [c]	Vibrational frequencies [d]
$FeMgSiO_4$	3.24	1.45×10^{-29}	4.97, 0.886, 0.884	98, 113, 220, 290, 366, 367, 518, 551, 627, 695, 711, 750, 770, 799, 931
$FeMgSiO_4^-$	6.22	8.65×10^{-29}	4.97, 0.865, 0.863	93, 105, 223, 281, 348, 366, 432, 526, 546, 600, 671, 715, 733, 879, 898

790 [a] In Debye (= 3.336 x 10^{-30} Cm). [b] In m^3. [c] In GHz. [d] In cm^{-1}.

791

792

Figure Captions.

Figure 1. Comparison of the atomic O profile measured by the NEMI instrument on HotPay 2, with the Na density measured by the ground-based ALOMAR Na lidar between 20:00 and 20:09 LT, immediately before the launch at 20:14 LT.

Figure 2. Comparison of the profiles of positive ions and electrons measured by an ion probe and Faraday rotation technique on HotPay 2, compared with the predictions of the plasma model (including a profile of negative ions).

Figure 3. Detection efficiency of the Dartmouth Dust Detector as a function of altitude and dust size for the HotPay 2 flight. Detector performance degrades significantly below 82 km. Peak detection efficiency above 85 km is ~0.8, with an average efficiency of ~0.5 over the 0.5 - 1.0 nm size range.

Figure 4. Vertical profile of negatively-charged aerosols measured by the Dartmouth Dust Detector on HotPay 2, compared with the prediction from the dusty plasma model. The difference between the measured positive ions and electrons (see Figure 2 for the profiles of these species) is also shown.

Figure 5. The temperature profile measured by the ALOMAR Na lidar between 20:00 and 20:09 LT, immediately before the HotPay 2 launch at at 20:14 LT. This profile is compared with the January mean profile predicted by the SOCRATES model. Also shown is the January mean profile of the vertical eddy diffusion coefficient, K_{zz}.

Figure 6. MSP concentration (particle cm^{-3}) as a function of height and radius, calculated for an ablated meteoric input of 5 t d^{-1}.

Figure 7. Probable structures of MSPs with sphere-equivalent radii of about ~0.3-0.5 nm. These examples include, from top to bottom, left-hand side: $FeMgSiO_4$ (olivine) dimer; $FeSiO_3$ (ferrosilite) trimer; and $MgSiO_3$ (enstatite) trimer. Right-hand side: MgOH and FeOH trimers. Calculations are at the B3LYP/6-311+g(2d,p) level of theory.

Figure 8. Modelled diurnal Na layer using the NaMOD 1D model, with the atomic O and temperature profiles constrained to the observed profile (Figure 1). The white broken line indicates the time of the HotPay 2 launch.

Figure 9. Modelled profiles of Na, $NaHCO_3$ and Na^+ for the conditions of the HotPay 2 launch, compared with the Na profile measured by the ALOMAR Na lidar.

Figure 10. Vertical profiles of positive, neutral and negatively charged MSPs in the three size ranges used in the model (MSP1, $r < 0.5$ nm; MSP2, $0.5 \leq r < 1.0$ nm; MSP3, $r \geq 1.0$ nm). The steady-state distributions are predicted by the dusty plasma model for the case of the plasma illustrated in Figure 2.

Figure 1.

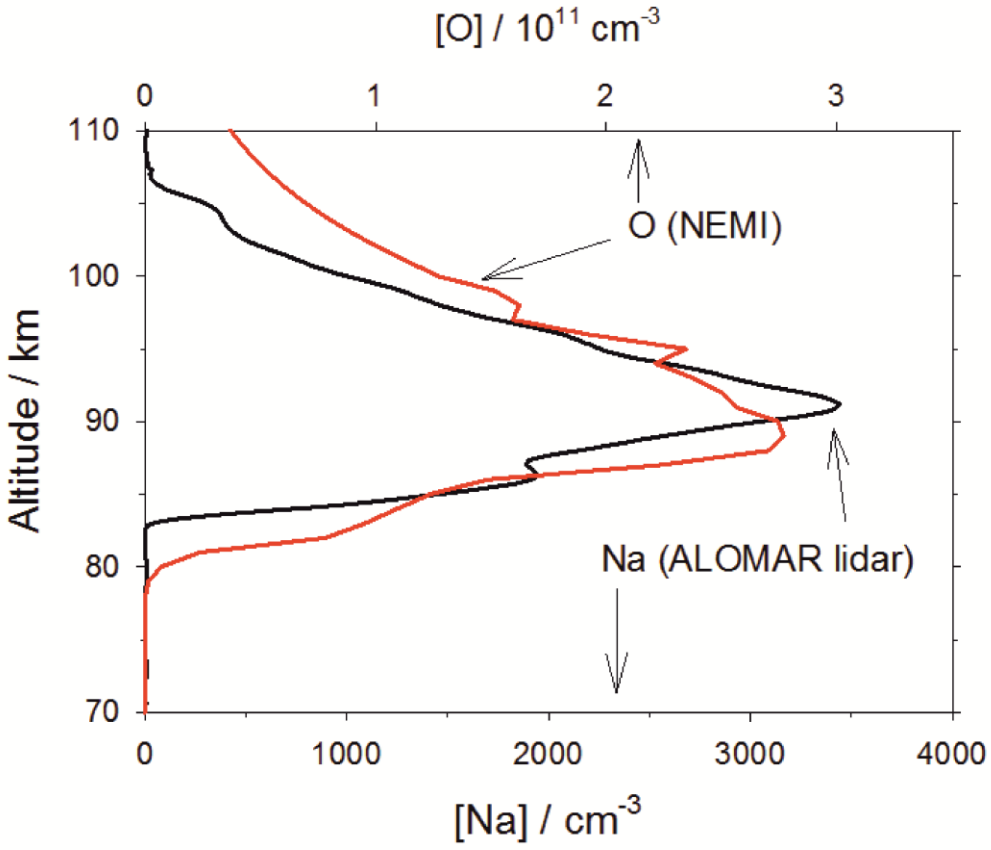

Figure 1. Comparison of the atomic O profile measured by the NEMI instrument on HotPay 2, with the Na density measured by the ground-based ALOMAR Na lidar between 20:00 and 20:09 LT, immediately before the launch at 20:14 LT.

Figure 2.

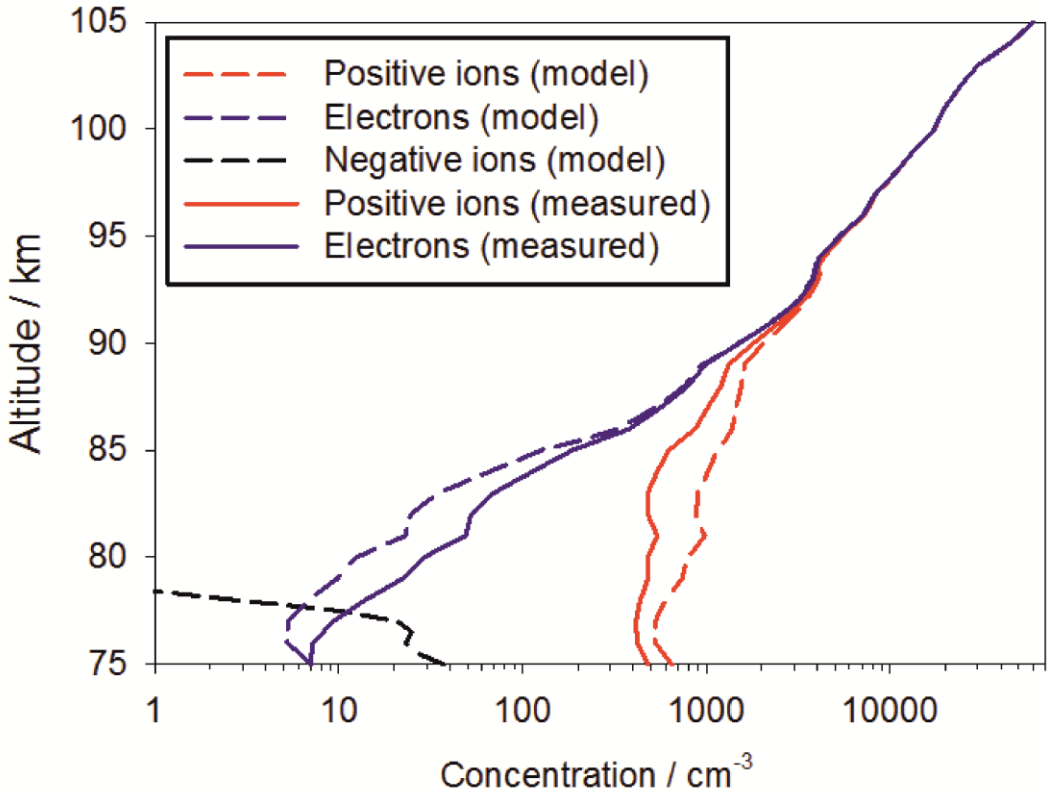

Figure 2. Comparison of the profiles of positive ions and electrons measured by an ion probe and Faraday rotation technique on HotPay 2, compared with the predictions of the plasma model (including a profile of negative ions).

873 **Figure 3.**
874
875

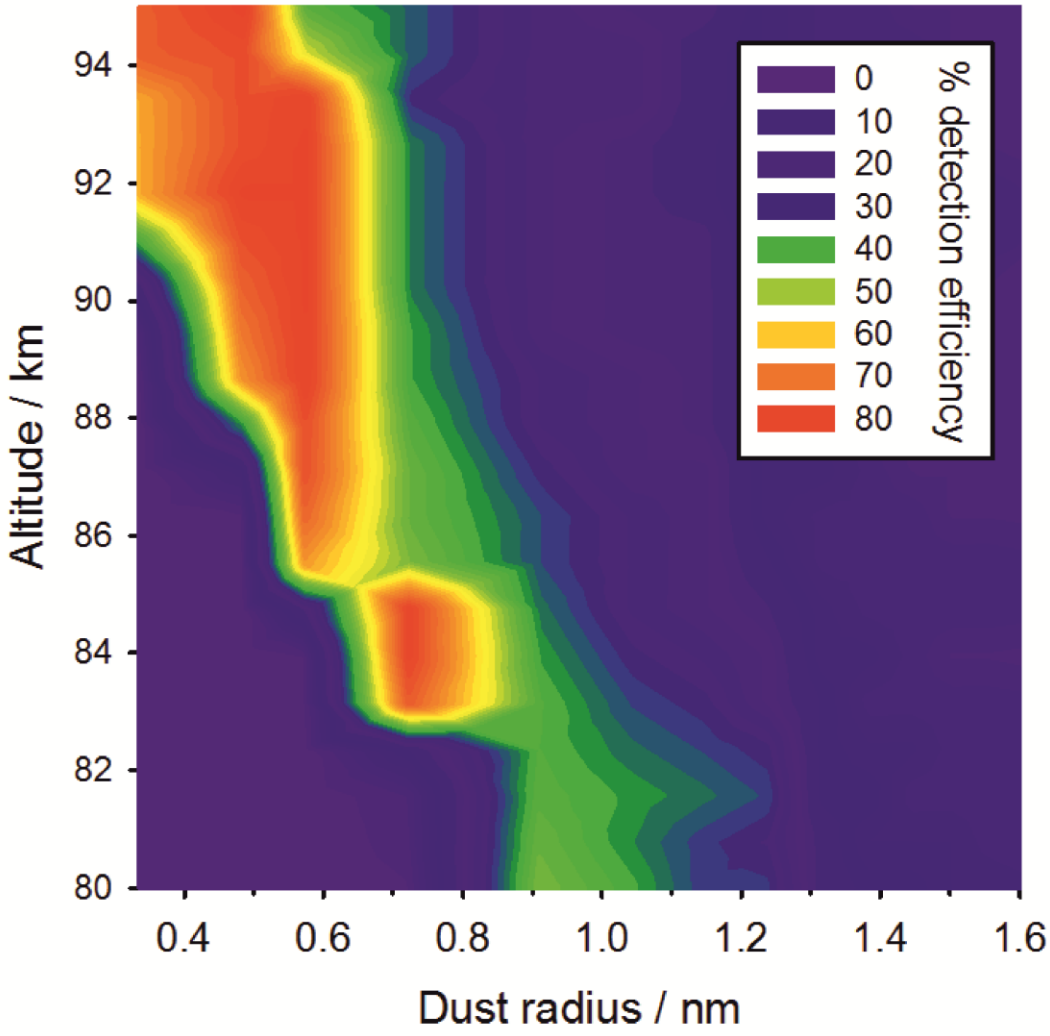

876

877 **Figure 3.** Detection efficiency of the Dartmouth Dust Detector as a function of
878 altitude and dust size for the HotPay 2 flight. Detector performance degrades
879 significantly below 82 km. Peak detection efficiency above 85 km is ~0.8, with an
880 average efficiency of ~0.5 over the 0.5 - 1.0 nm size range.

881

Figure 4.

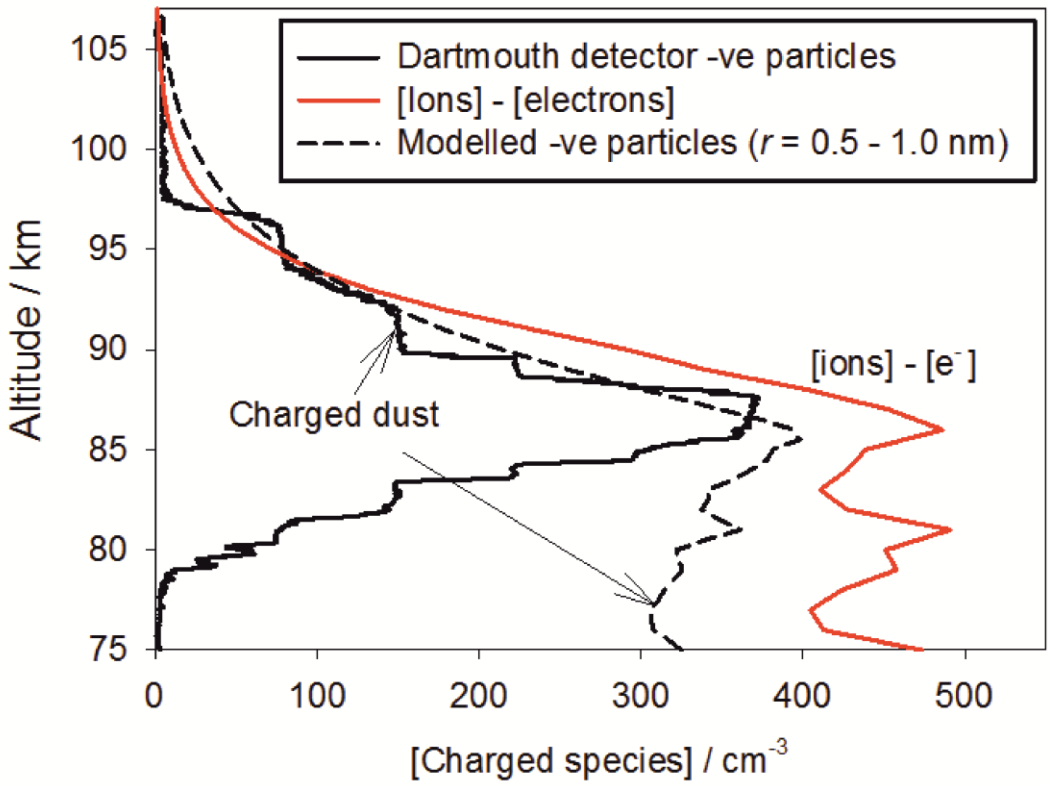

Figure 4. Vertical profile of negatively-charged aerosols measured by the Dartmouth Dust Detector on HotPay 2, compared with the prediction from the dusty plasma model. The difference between the measured positive ions and electrons (see Figure 2 for the profiles of these species) is also shown.

899 **Figure 5.**

900

901

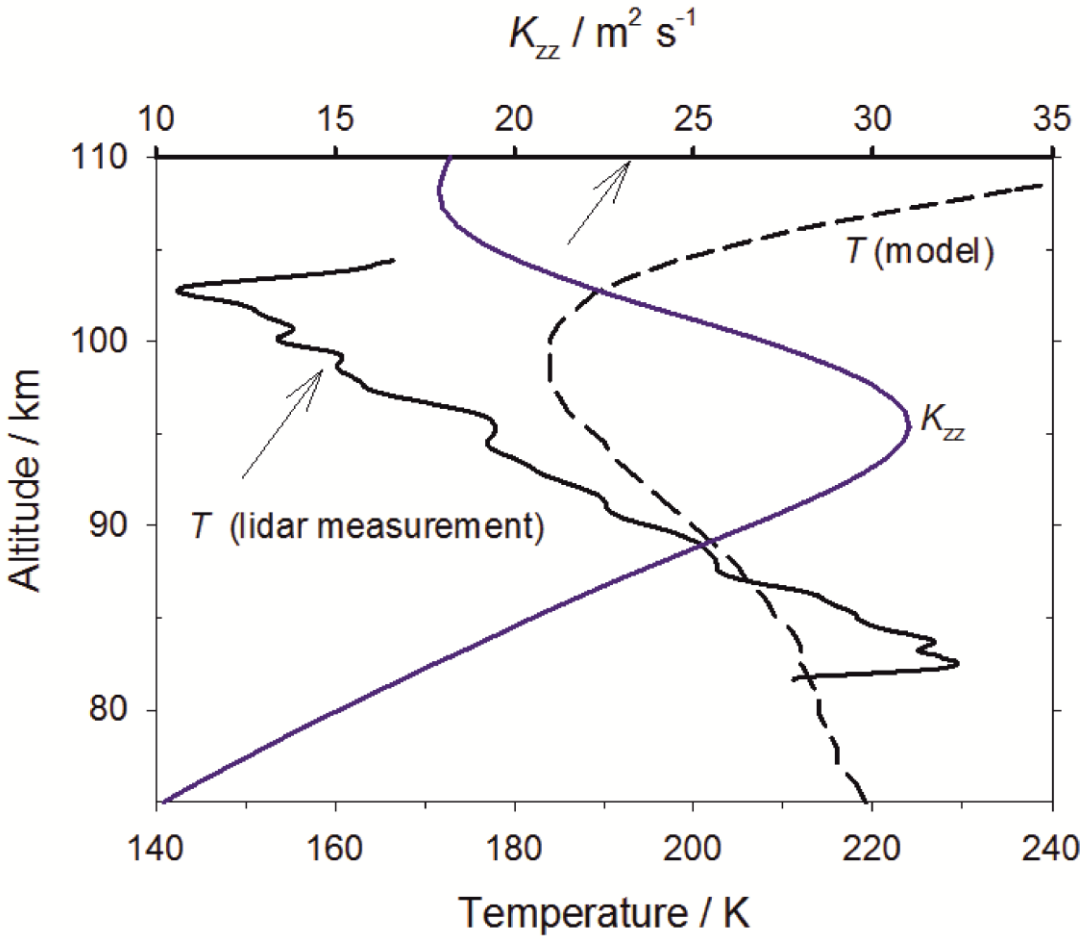

902

903

904

905

906 **Figure 5.** The temperature profile measured by the ALOMAR Na lidar between
907 20:00 and 20:09 LT, immediately before the HotPay 2 launch at at 20:14 LT. This
908 profile is compared with the January mean profile predicted by the SOCRATES
909 model. Also shown is the January mean profile of the vertical eddy diffusion
910 coefficient, K_{zz}.

911

912

913 **Figure 6.**

914

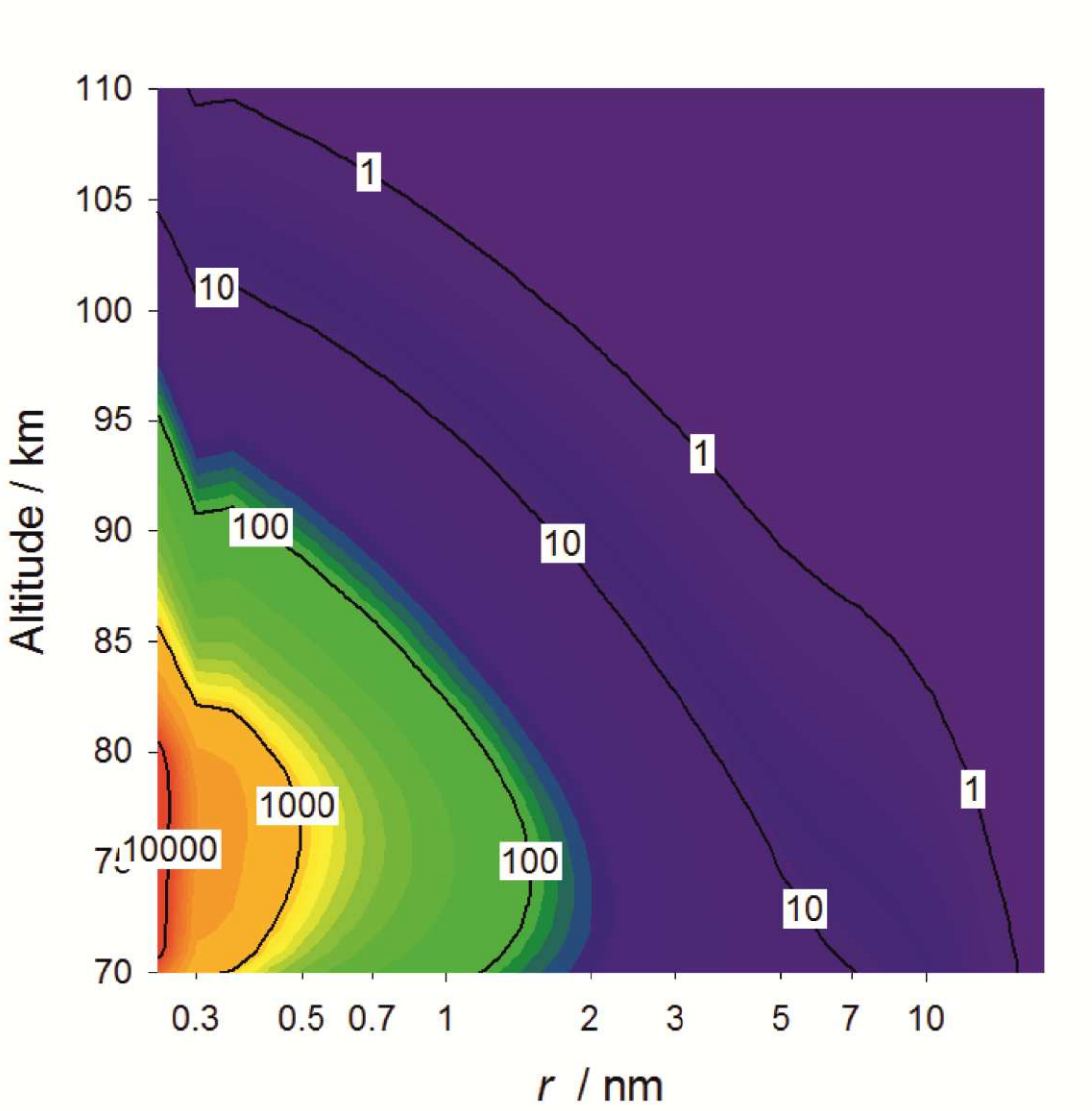

915

916

917

918

919

920

921

922 **Figure 6.** MSP concentration (particle cm^{-3}) as a function of height and radius,
923 calculated for an ablated meteoric input of 5 t d^{-1}.

924

925

Figure 7.

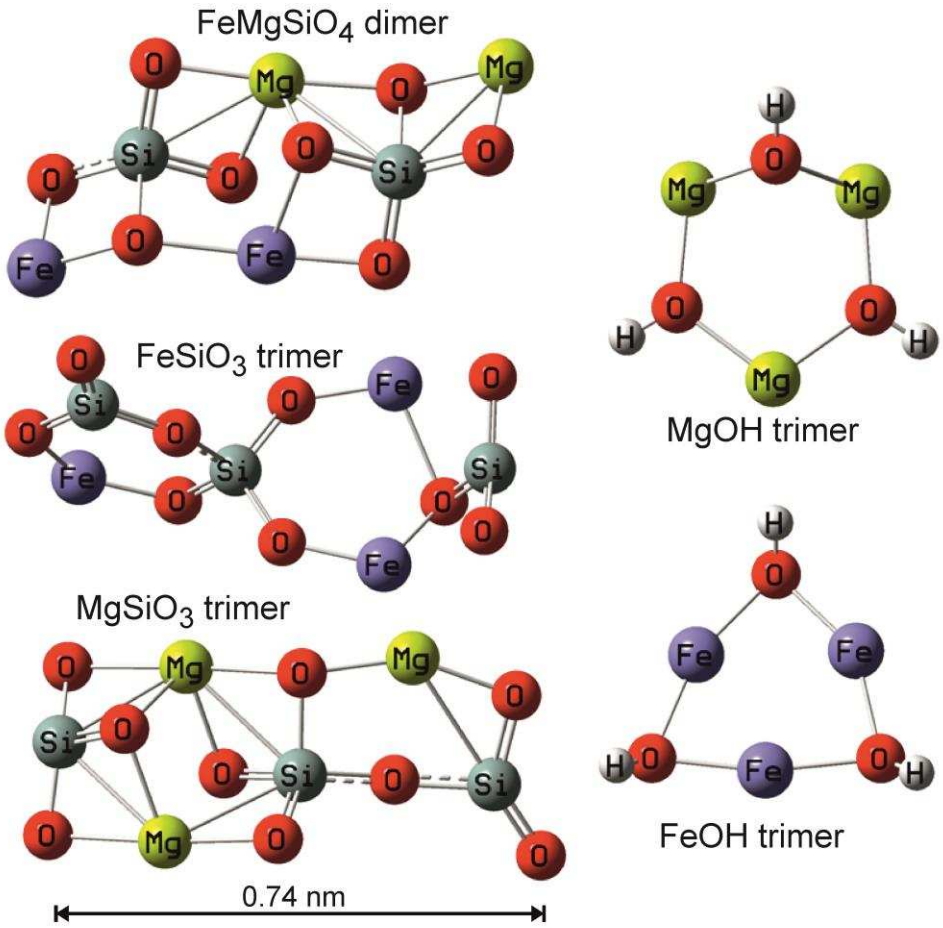

Figure 7. Probable structures of MSPs with sphere-equivalent radii of about ~0.3-0.5 nm. These examples include, from top to bottom, left-hand side: $FeMgSiO_4$ (olivine) dimer; $FeSiO_3$ (ferrosilite) trimer; and $MgSiO_3$ (enstatite) trimer. Right-hand side: MgOH and FeOH trimers. Calculations are at the B3LYP/6-311+g(2d,p) level of theory.

946 **Figure 8.**

947

948

949

950

951

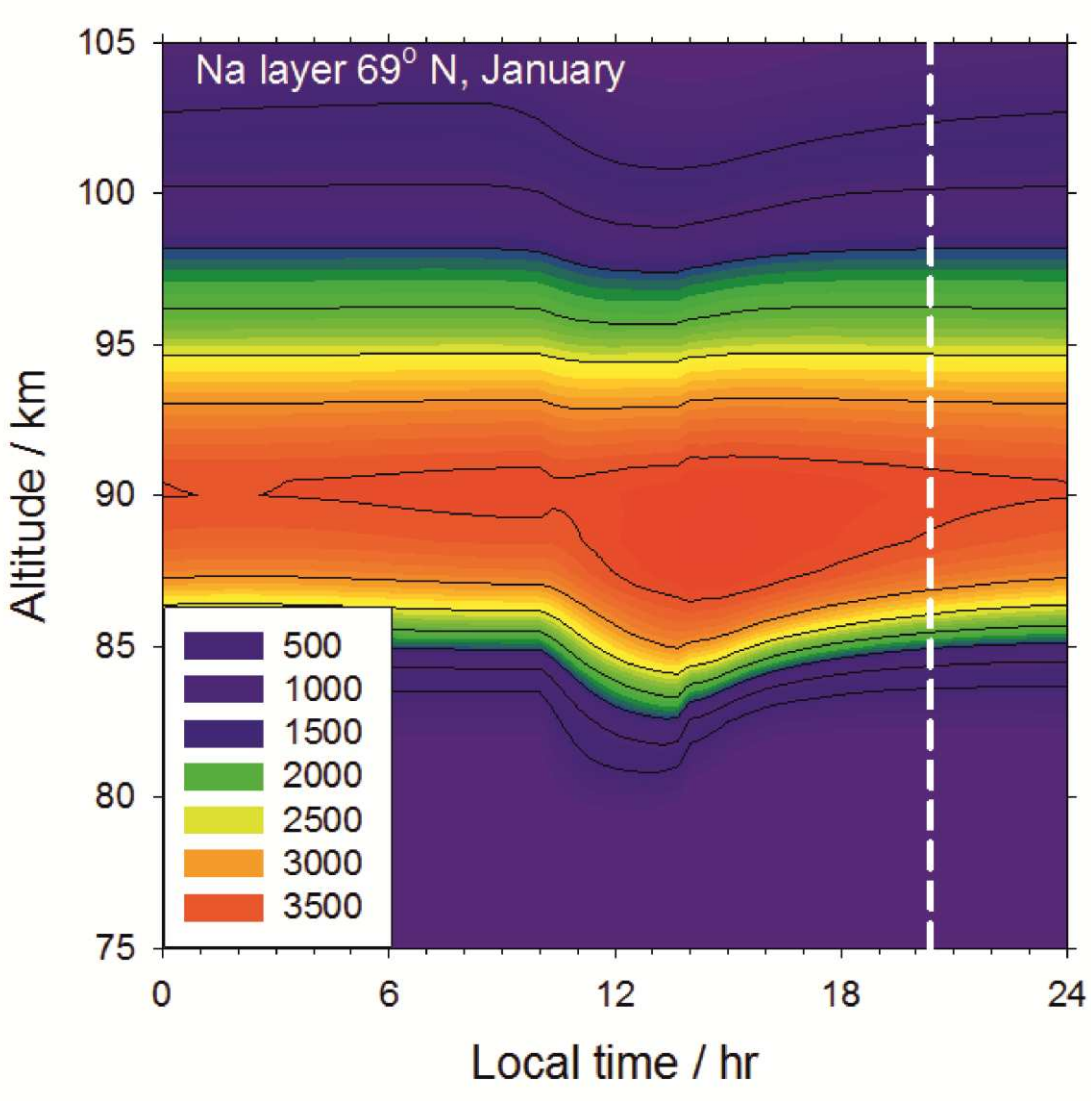

952

953

954 **Figure 8.** Modelled diurnal Na layer using the NaMOD 1D model, with the atomic O
955 and temperature profiles constrained to the observed profile (Figure 1). The white
956 broken line indicates the time of the HotPay 2 launch.

957

958

959

960

961 **Figure 9.**

962

963

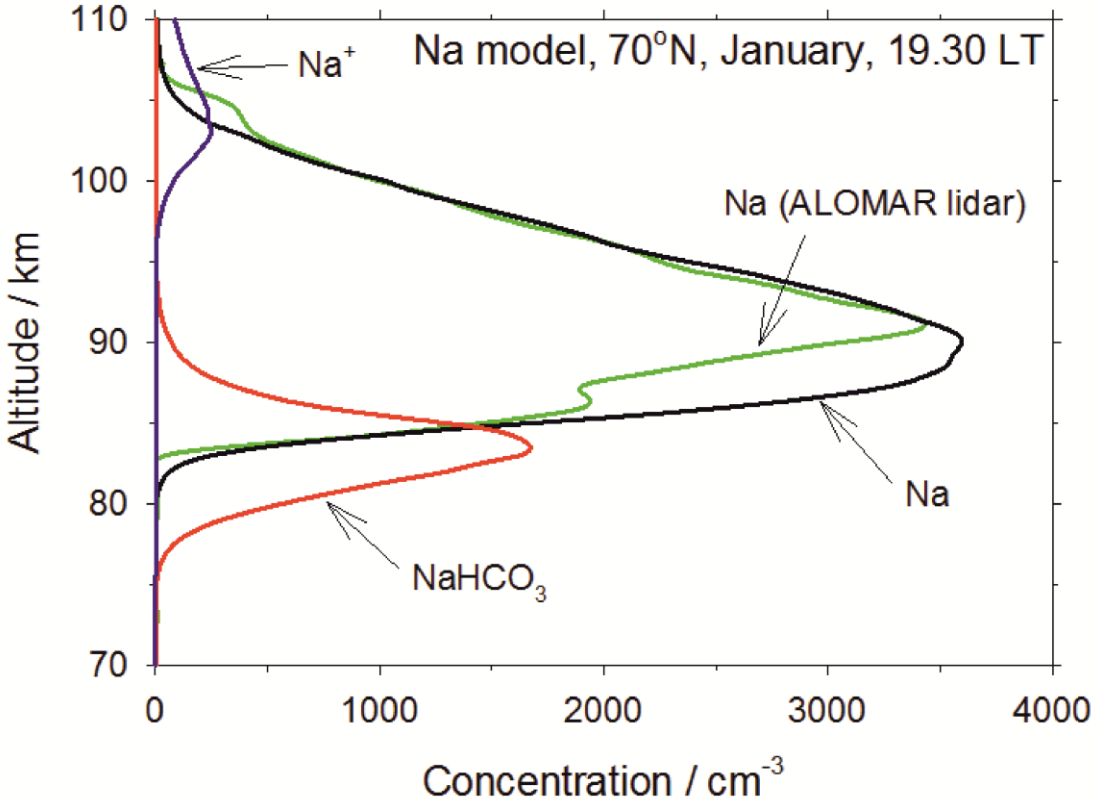

964

965

966

967 **Figure 9.** Modelled profiles of Na, $NaHCO_3$ and Na^+ for the conditions of the HotPay
968 2 launch, compared with the Na profile measured by the ALOMAR Na lidar.

969

970

971

972

973
974 **Figure 10.**
975

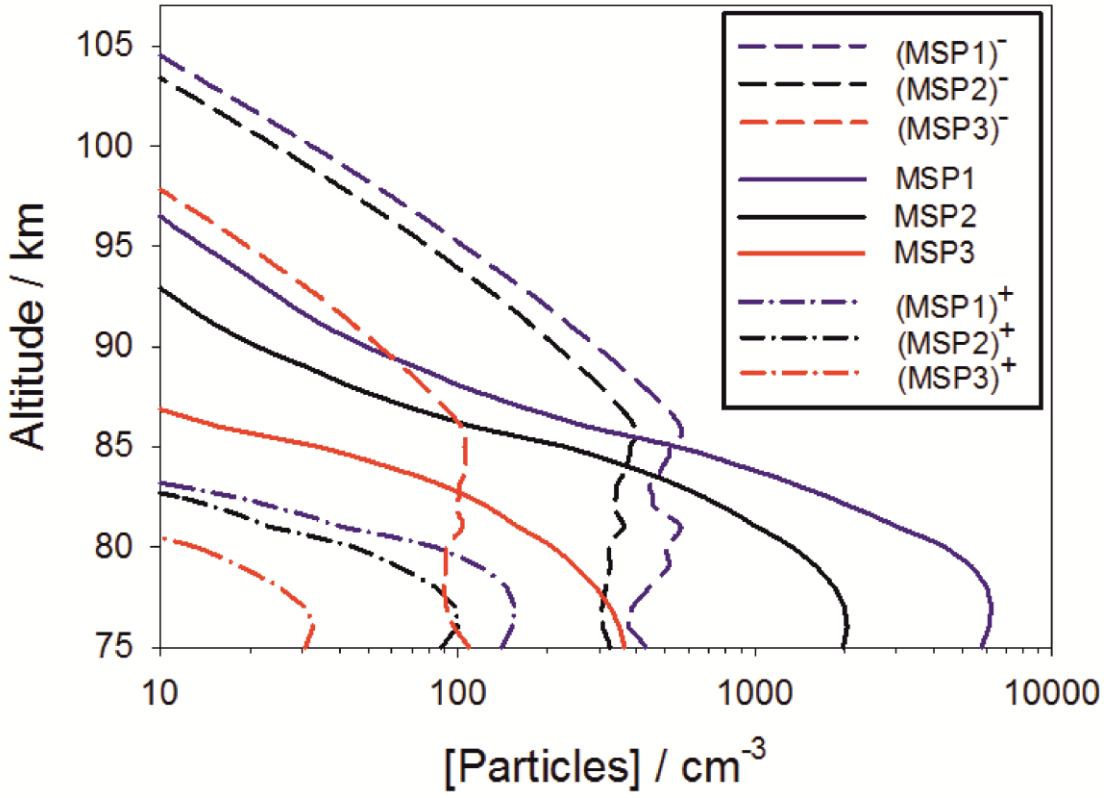

976
977
978
979 **Figure 10.** Vertical profiles of positive, neutral and negatively charged MSPs in the
980 three size ranges used in the model (MSP1, $r < 0.5$ nm; MSP2, $0.5 \leq r < 1.0$ nm;
981 MSP3, $r \geq 1.0$ nm). The steady-state distributions are predicted by the dusty plasma
982 model for the case of the plasma illustrated in Figure 2.
983
984
985